communications materials

Article

https://doi.org/10.1038/s43246-024-00491-7

The role of stacking fault tetrahedra on void swelling in irradiated copper

Ziang Yu [1], Yan-Ru Lin [2], Michael J. Zachman [3], Steven J. Zinkle [1,2,4] & Haixuan Xu [1]

A long-standing and critical issue in the field of irradiated structural materials is that void swelling is significantly higher in face-centered cubic-structured (fcc) materials (1% dpa^{-1}) as compared to that of body-centered cubic-structured (bcc) materials (0.2% dpa^{-1}). Despite extensive research in this area, the underlying mechanism of the difference in swelling resistance between these two types of materials is not yet fully understood. Here, by combining atomistic simulations and STEM imaging, we find stacking fault tetrahedra (SFTs) are the primary cause of the high swelling rate in pure fcc copper. We reveal that SFTs in fcc copper are not neutral sinks, different from the conventional knowledge. On the contrary, they are highly biased compared to other types of sinks because of the SFT-point defect interaction mechanism. SFTs show strong absorption of mobile self-interstitial atoms (SIAs) from the faces and vertices, and weak absorption of mobile vacancies from the edges. We compare the predicted swelling rates with experimental findings under varying conditions, demonstrating the distinct contributions of each type of sink. These findings will contribute to understanding the swelling of irradiated structural materials, which may facilitate the design of materials with high swelling resistance.

Void swelling at intermediate temperatures, occurring at approximately 0.3−0.6 of the melting temperature, is widely observed in structural materials exposed to high levels of particle radiation[1–4]. Such a phenomenon leads to significant effects that result in unacceptable volumetric changes, degraded mechanical performance, and a limited lifetime of structural components in nuclear reactors[4–7] and other extreme environments, such as space vehicles[8]. Furthermore, the underlying cause—defect interaction in materials—is a critical focus in numerous significant fields, such as high entropy alloys[9], energy storage materials[10], and perovskites[11]. One critical observation is that swelling rates are generally much higher in fcc materials as compared to bcc materials[5,6,12,13], with a few exceptions[14]. Because of the critical significance of such differences, the underlying reason has received significant attention and generated extensive discussions in recent decades. However, a conclusive explanation is yet to be established[15], although multiple mechanisms have been proposed by previous studies.

Among these mechanisms, defect accumulation and the effect of microstructures in irradiated bcc and fcc metals has garnered the most attention[16]. Previous studies[17,18] indicate that to create the same level of defect density, Fe requires a dose that is two to three orders of magnitude higher than Cu. Additionally, the difference in defect clustering during the thermal spike phase between fcc and bcc metals[19] has been suggested as a contributing factor, but a fundamental understanding of how these factors influence the swelling behavior has not been established. Some other effects, like the glissile self-interstitial atom (SIA) cluster removal mechanism[13,20,21], which affects the survival fraction of defects from displacement cascades[22], are also considered. Nevertheless, none of the models are capable of reproducing the experimental values of swelling rates at different temperatures in irradiated materials. Moreover, microstructural features, such as dislocations, act as the sinks of mobile point defects[4], and the bias model[23,24] has been established to quantify the void swelling. Specifically, dislocation bias has been extensively discussed[4,23–26], but the difference between bias factors obtained in fcc and bcc materials cannot fully explain their swelling rate difference. Nevertheless, it is clear that the effect of microstructural features is the critical factor to investigate these phenomena, and the model to study swelling behaviors must consider the types and densities of the sinks formed during the irradiations. However, due to the complexity of irradiation conditions, identifying the primary underlying cause of the observed difference in swelling behavior between fcc and bcc materials presents a significant challenge.

[1]Department of Materials Science and Engineering, The University of Tennessee, Knoxville, TN 37996, USA. [2]Materials Science and Technology Division, Oak Ridge National Laboratory, Oak Ridge, TN 37831, USA. [3]Center for Nanophase Materials Sciences, Oak Ridge National Laboratory, Oak Ridge, TN 37831, USA. [4]Department of Nuclear Engineering, The University of Tennessee, Knoxville, TN 37996, USA. e-mail: xhx@utk.edu

Among all the major types of microstructural features in fcc Cu, this study identifies SFTs (mostly between 1.5 and 3.5 nm[27–29]) as a significant cause of the swelling rate differences between fcc and bcc materials, based on state-of-the-art mesoscale and atomistic kinetic Monte Carlo (AKMC) simulations[30,31]. SFTs have been long considered neutral sinks for vacancy and SIA point defect absorption due to the low elastic strain associated with the stair-rod dislocations that comprise the SFT periphery[32]. We observe both perfect and non-perfect SFTs[27] to be non-neutral sinks that prefer to absorb mobile SIAs over mobile vacancies in fcc copper. Such a phenomenon is due to the underlying mechanism of the SFT-point defect interaction, showing strong absorption of mobile SIAs from the faces and vertices of the SFT, and weak absorption of mobile vacancies from the edges of the SFT. This mechanism leads to higher bias values of SFTs compared to other types of sinks in irradiated copper[26], including straight dislocations (both edge and screw types), 1/3<111> interstitial loops, and voids. The high bias values of SFTs, coupled with high number densities (higher than 10^{22} m^{-3} based on experimental observations under 600 K[12,28,29,33–36]), collectively result in the high sink strength of SFTs. We further analyze the effects of each type of sink on void swelling phenomena based on the obtained sink strengths and predicted swelling rates and compare computational results with a large number of neutron- or ion-irradiation experiments, with different irradiation conditions and material microstructures[12,29,33–49]. We demonstrate that SFTs are the primary cause of high swelling rates in irradiated fcc copper and play a decisive role in creating the observed differences in swelling rates between general fcc and bcc structural materials.

These findings challenge traditional beliefs that SFTs do not act as biased sinks in irradiated fcc materials. Moreover, the insights gained from this study represent a significant step towards understanding the roles of different sinks on swelling behavior, which in turn can inform the development of materials with enhanced swelling resistance. For example, one possible approach to achieve improved swelling tolerance could involve reducing the density of small SFTs (≤3.5 nm in size), e.g. through tuning stacking fault energies or compositional complexity. Additionally, increasing the initial dislocation density by cold working will also influence the swelling behavior of fcc materials. These strategies could potentially lead to the development of more robust fcc structural materials capable of withstanding high-dose irradiations and being more resistant to irradiation-induced swelling.

Results and discussion

Mechanisms of SFT-point defect interactions

The mechanism of SFT-point defect interaction was quantified from statistical analysis of the diffusion behavior of mobile point defects near an SFT. Contrasting behavior occurred for SIAs and vacancies due to the varying stress/strain field in the matrix surrounding the SFT. We find that mobile SIAs are absorbed at the faces and vertices of SFTs, corresponding to regions with tensile strains; mobile single vacancies are absorbed at the edges of SFTs, corresponding to regions with compressive strains. The volumetric strain map of a 2 nm SFT is shown in Fig. 1a, b, where regions under tension appear in red and are normal to the faces and around vertices of the SFT, and regions under compression appear in blue and are normal to the SFT edges. Such a pattern persists over long distances (greater than 10 nm) and is indicated in light yellow and light blue. Please note that, as the strain fields are identical on each face of the SFT, only the top face has been chosen to clearly illustrate the 3-D properties. The schematic representation of this is depicted in Fig. 1b (from another angle of Fig. 1a).

To clearly represent the varying SFT-point defect interaction, we depict the diffusion tendency of point defects around a 2 nm SFT in Fig. 1c, d for SIAs and vacancies, respectively. Diffusion tendency was obtained based on KMC simulations at 100 K, showing the expected diffusion direction and its probability of a mobile point defect at every atomic position near the SFT. The simulation at 100 K captures the key diffusion direction produced during irradiation at higher temperatures. Here, the expected diffusion direction is represented by the vector sum of the diffusive steps taken from a given atomic position, and the probability corresponds to the length of this resultant vector relative to the combined lengths of all diffusive step vectors. To enhance the clarity of the figure, such vectors are represented using spheres. In Fig. 1c, the attractive (tensile) regions (labeled in yellow and red) show the diffusion direction of SIAs toward the SFT, and the repulsive regions are labeled in green and blue. The size of the sphere represents the probability of an SIA diffusing along that pathway, showing a consistent tendency but a weaker effect over long ranges. The magnitude of the interaction with the SFT is much weaker for vacancies than that for SIAs. Figure 1d shows that the SFT-vacancy interaction is very strong only at very short ranges (1−2 nm). Attractive pathways are found within 1 nm next to the edges of SFTs; conversely, repulsive pathways are predominant at many geometric locations for the SFT-vacancy interaction. This contrasting interaction behavior, along with the high SFT number densities observed in irradiated Cu that shortens the average distance between mobile point defects and SFTs, leads to a high effectiveness of SFTs as a sink for mobile SIAs in copper.

This observed mechanism can explain the results of several previous experimental studies and theoretical calculations. SFTs were originally suggested to collapse by absorbing a sufficient number of SIAs[32,50] in irradiated fcc materials. Later, the annihilation of SFTs as a result of irradiation was confirmed by in-situ observations in fcc materials[51,52], and the growth/shrinkage mechanisms were attributed to the absorption of mobile point defects[27,50]. Here, we observed a high preference for SFTs to absorb SIAs over vacancies, which will lead to significant shrinkage of SFTs. This observation further clarifies why SFTs rarely grow beyond 3.5 nm in size as they form in cascades. Additionally, a possible growth mechanism involving migration and coalescence of small SFTs (15-vacancy SFT) was proposed by Martinez et al.[53] based on molecular dynamic (MD) simulations between 600 K and 1000 K.

Experimental SFT lattice strain measurement

SFTs appear as bright triangular shapes when imaged along a ⟨110⟩ zone axis by low-angle annular dark-field scanning transmission electron microscopy (LAADF-STEM) (Fig. 2a), indicating the possible presence of strain[54]. Local lattice strain in the plane perpendicular to the incident beam direction can be determined by tracking changes in Bragg disk positions in convergent-beam electron diffraction (CBED) patterns (Fig. 2c) as a function of real space STEM probe position. Two-dimensional maps of strain can therefore be produced by measuring Bragg disk shifts in a rectangular array of positions across the sample. Here, we used a novel 4D-STEM method with exit-wave power-cepstrum (EWPC) analysis[55], which is robust to small sample mis-tilts and reciprocal space intensity variations such as those caused by dynamical diffraction, to extract strain information from such an array of CBED patterns (Fig. 2c). As Fig. 2b illustrates, experimental EWPC-STEM data of dual-ion-irradiated copper reveals a distribution of tensile areal strain (approximately $\varepsilon_{xx} + \varepsilon_{yy}$) inside and surrounding an SFT. For comparison with the results of the simulation in Fig. 1, a rotation was applied to match the experimental orientation and averaging the strain within the thickness that encompassed the entire tetrahedral SFT in the $[1\bar{1}0]$ direction (Fig. 2f). The resulting areal strain distribution (Fig. 2e) qualitatively matches the experimental strain map (Fig. 2b) fairly well, given the additional experimental noise and sub-nm in-plane spatial resolution, showing higher tensile strain in the upper left SFT vertex than the two others, and reduced stress immediately outside of this vertex. Additionally, the dependence of SFT strain field on size is qualitatively similar, although the predicted spatial extent of the strain field will be lessened for smaller SFTs.

One difference between the experimental and simulated results is that the two other vertices also exhibit a tensile strain in the experimental results, while they do not in the simulated results (Fig. 2e), which may be due to the finite probe size or differences in averaging mechanisms. Quantitatively, the maximum experimental and simulated tensile areal strains are on the same order of magnitude as well, at approximately 3.5% and 1.5%, respectively. Our simulation did not account for the influence of helium (which can be generated in a real nuclear reactor environment from nuclear transmutation

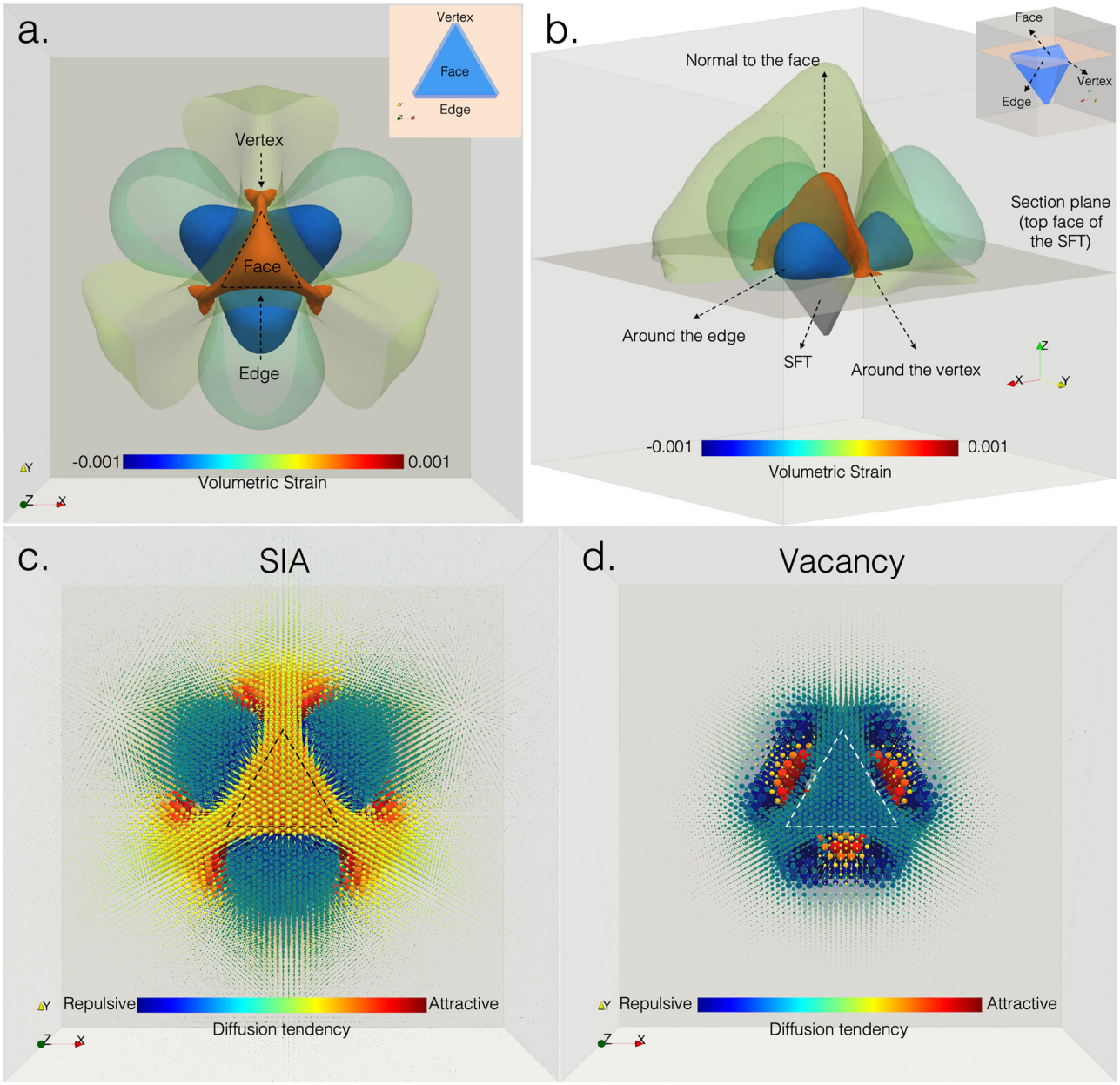

Fig. 1 | Top view of the SFT strain field and diffusion tendency of SIAs. **a** Volumetric strain field of a 2 nm SFT (top view). **b** Another perspective of the SFT strain field. The scheme of the SFT for both (**a**) and (**b**) are respectively shown in the top right corner inset figures. Diffusion tendency of an SIA (**c**) and a vacancy (**d**) around a perfect 2 nm SFT based on KMC simulations are provided for comparison with (**a**) from the same orientation. The color represents the expected diffusion direction, and the size of the spheres represents the expected probability of the diffusion path. Complete 3-D rotational movies are provided in the Supplementary Information.

reactions) on the SFT strain field, however, which could potentially increase the strain induced through pressure effects. The differences in strain distribution observed in the experimental and simulated results for the two vertices on the right (Fig. 2b, e) and the overall maximum strain differences may therefore also be related to implantation of helium atoms in the experimental sample. Despite these small differences, EWPC-STEM strain mapping lends support to the findings of the simulation, indicating that SFT's have a relatively large tensile strain and therefore an affinity for mobile SIAs.

SFT bias and comparison with other sinks

The mechanisms of SFT-point defect interactions lead to the preferential absorption of mobile SIAs over vacancies, which is termed bias. We quantified the bias values of SFTs, dislocation loops, and straight dislocations using the same AKMC approach. Both bias equations and the AKMC framework are elaborated in the Methods Section. The results are shown in Fig. 3 and demonstrate that the bias for both perfect and imperfect SFTs is the highest among all major sinks that exist in irradiated copper.

Since SFT sizes observed in neutron-irradiated copper are mostly between 1.5 nm and 3.5 nm based on experimental observations[27–29], the bias values of 1.5 nm, 2 nm, and 3.5 nm perfect SFTs (with 21, 36, and 105 vacancies) were calculated and are shown in Fig. 3a. Within the experimentally observed SFT number densities in the void swelling temperature regime (between 10^{18} m^{-3} and 10^{23} m^{-3}[3,12,28,29,42,56,57]), the perfect SFT bias is found between 0.54 and 0.75. The bias decreases with rising temperatures from 573 K to 673 K and decreases with increasing SFT sizes from 1.5 nm to 3.5 nm. Such size dependence is also supported by a previous binding energy calculation[58]. For non-perfect SFTs, we select an intermediate size of

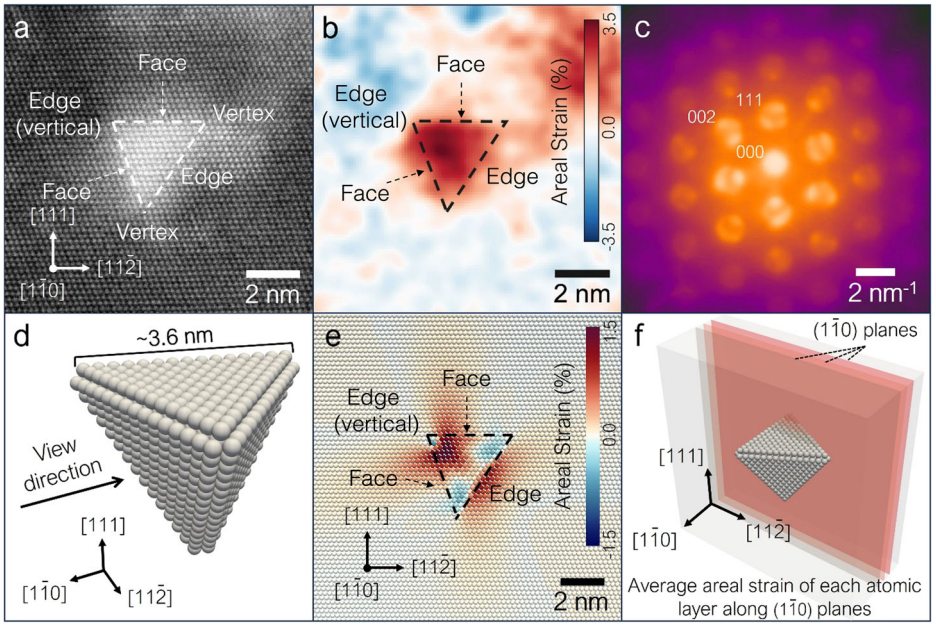

Fig. 2 | Comparison of experimental and simulated SFT areal strain. a Atomic-resolution LAADF −STEM image of an SFT in dual-ion-irradiated Cu at 440 °C to 30 dpa and 48 appm He. **b** Areal strain perpendicular to the beam direction measured by 4D-STEM EWPC method. **c** Average CBED pattern in the region of the SFT. **d** Crystal structure of the SFT used for simulation calculation. **e** Areal strain averaged over the SFT strain field in the $[1\bar{1}0]$ direction. **f** Schematic diagram of the areal strain averaging method used for the simulated results. Faces, edges, and vertices of the SFT are labeled in (**a**), (**b**), and (**e**) for comparison with Fig. 1. Notice that the Edge (vertical) refers to an edge that is vertical to the view plane, and the labels for vertices in (**b**) and (**e**) are hidden for a clearer view.

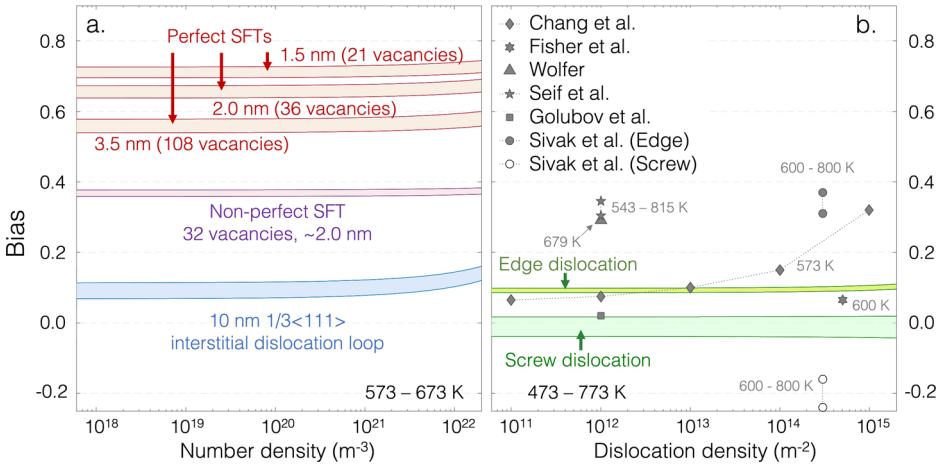

Fig. 3 | Bias of different types of sinks based on theoretical calculations. a SFT bias with different sizes (in red bands) between 573 and 673 K. Non-perfect SFT (32 vacancies, ~2 nm) bias is also included and labeled in a purple band. 1/3<111> interstitial loop bias (10 nm size) is labeled in a blue band. **b**. Dislocation bias from this study (473–773 K) and the comparison with previous works, mostly between 500 K and 800 K. Edge dislocation bias is labeled with a yellow band, and screw dislocation bias is labeled with a green band. Dislocation bias values calculated by previous works are labeled in filled markers (edge dislocations) and open markers (screw dislocations).

approximately 2 nm (with 32 vacancies) for our calculation. The bias values of non-perfect SFTs are found to be between 0.36 and 0.38 at the same temperature and density range as the perfect SFTs, shown in Fig. 3a. Our results reveal a significantly lower bias of non-perfect SFTs compared to perfect SFTs at the same size, temperature, and number density. This phenomenon can be attributed to the inability of non-perfect SFTs to form four vertices as perfect SFTs do. Since this study has demonstrated that vertices play a critical role in absorbing mobile SIAs and repulsing mobile vacancies, the absorption region of mobile SIAs is thus much smaller in non-perfect SFTs than in perfect ones.

The bias of a 1/3<111 > {111} interstitial loop was calculated to be around 0.1 between 573 K and 673 K as shown in Fig. 3a. Since the typical diameter of loops is larger than 5 nm and increases up to ~30 nm with increasing irradiation doses in experiments[29,33,59,60], a 10 nm loop was employed in this study. Similarly, the dislocation bias values of both edge and screw types were found to be much lower than those of SFTs, labeled in yellow and green bands in Fig. 3b. Edge dislocation bias is shown between 0.08 and 0.1 with the commonly reported dislocation density between 10^{12} m^{-2} and 10^{13} m^{-2} in experiments[12,29,34–36,41–44,61]. Plus, it is not sensitive to the temperature change from 473 K to 773 K, during which the swelling phenomenon occurs. The obtained bias for edge dislocations is in good agreement with previous works, including atomistic simulations by Chang et al.[62], elasticity theory calculations by Skinner et al.[63] and Fisher et al.[64], and the production bias model by Golubov et al.[59]. Alternatively, Wolfer[20], Seif et al.[65], and Sivak et al.[66] reported relatively high dislocation bias values around 0.3. However, the highest edge dislocation bias listed above is still lower than that of SFTs. In comparison, screw dislocation bias exhibits much lower bias values, ranging from −0.04 to 0.02 as the temperature is raised from 473 K to 773 K. The negative values were also reported by Sivak et al.[66], suggesting that screw dislocations in fcc copper are less effective at absorbing mobile SIAs compared to edge dislocations. Detailed bias values from 473 K to 773 K for all major sinks are provided in Supplementary Fig. 7 to 12.

Swelling rates and effects of major sinks

The swelling rate in irradiated copper is determined by calculating the sink strength of all major sinks, as elaborated in the Methods Section. The obtained results are compared with experimentally reported swelling rates under irradiations[12,29,33–49], as shown in Fig. 4, where they are plotted as a function of irradiation temperature. These experimental results cover a wide range of conditions, including irradiation doses from 0.001 dpa to 150 dpa, and temperatures between 473 K and 802 K. We examine the contributions of each type of sink to the swelling phenomena and subsequently identify three primary scenarios. The violet curve represents the SFT-dominant

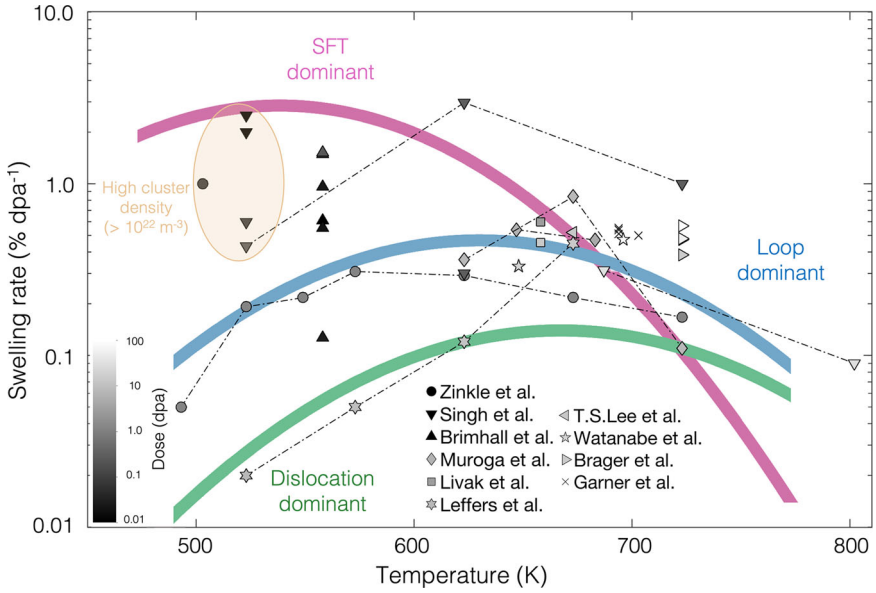

Fig. 4 | Comparison between predicted swelling rates and experimental observations. Three scenarios are provided. SFT-dominant scenario (i) is labeled by the violet curve, loop-dominant scenario (ii) is labeled by the blue curve, and dislocation-dominant scenario (iii) is labeled by the green curve. Edge dislocations and screw dislocations are considered 50%–50% in scenario (iii). For experimentally reported data, colors from black to white represent different doses from <0.01 dpa to 150 dpa (shown in log scale). Darker shades denote lower doses, which typically correspond to lower irradiation temperatures.

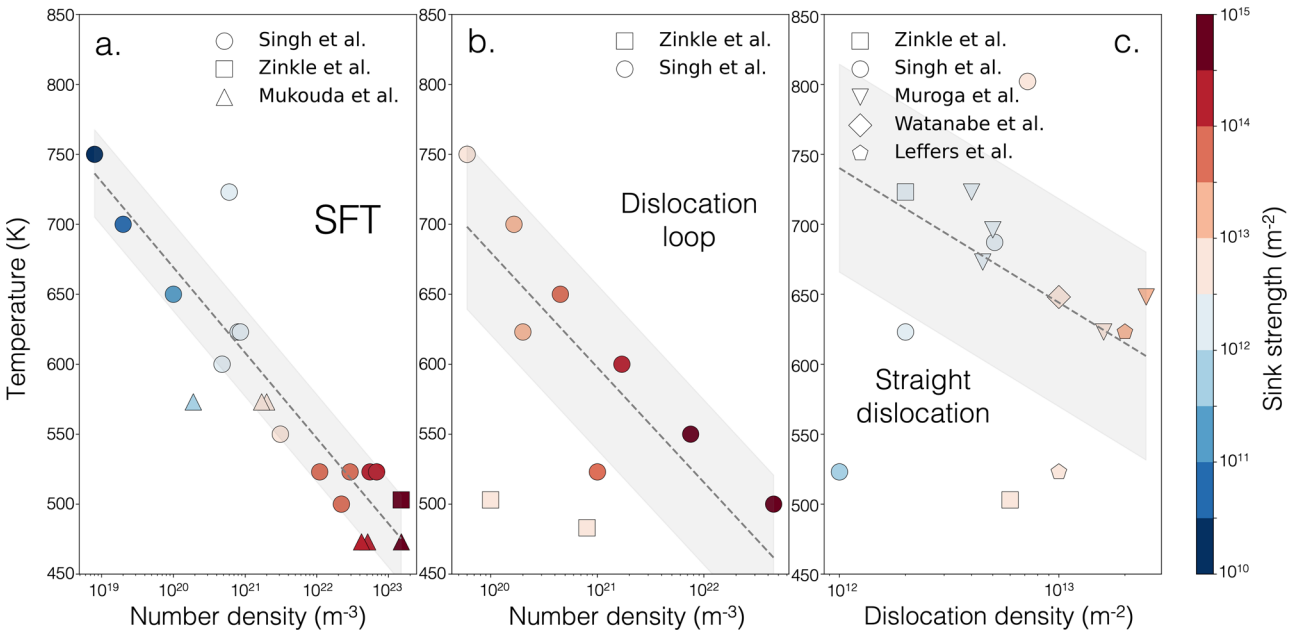

Fig. 5 | Calculated sink strengths of SFTs, dislocation loops, and straight dislocations. Results in this figure are obtained based on experimentally observed densities and temperatures[12,29,33–36,42–44,47,49,57,61] using the equation provided in the Methods Section for **a** SFTs, **b** dislocation loops, and **c** dislocations. Dislocation loop type is assumed to be 1/3<111>{111} interstitial and straight dislocation in (**c**) is 50% edge type and 50% screw type (both dissociates to two Shockley 1/6<112> partials). The shaded band shows the root mean square error (RMSE) of the fitting. Note that the data of "non-SFT clusters" provided by Singh and Zinkle[57] is assumed as representing 50% interstitial loops for estimations in (**b**). Dislocation density reported in two of the experimental studies by Singh et al.[35,42] is not considered for the fitting process.

scenario (i), the blue curve stands for the loop-dominant scenario (ii), and the green curve corresponds to the dislocation-dominant scenario (iii). The predicted swelling rates in these scenarios are calculated based on the sink strength of SFTs, loops, dislocations, and voids. The equations for sink strengths and swelling rates are provided in the Methods Section. Each scenario illustrated in Fig. 4 is derived based on the fitted sink density of experimental observations[12,29,33–36,42–44,47,57,61]. These fitted sink densities are represented by dotted lines in Fig. 5a–c for SFTs, loops, and dislocations, respectively. The fitted void density and size are provided in Supplementary Figs. 5 and 6.

In Scenario (i), SFTs serve as the dominant sink, corresponding to the upper limit of swelling rates (~1% dpa^{-1}) in neutron-irradiated copper. This scenario typically occurs under 600 K, at which the high densities of SFTs are observed in experiments (around 10^{22} m^{-3} or more)[12,28,29,33–36], as shown in Fig. 4. In this scenario, the sink strengths of SFTs for SIAs are mostly higher than 10^{13} m^{-2} (Fig. 5a), which are higher than those of straight dislocations (Fig. 5c). Such high SFT sink strengths are due to the calculated high bias values and the experimentally observed high SFT number densities under 600 K (>10^{21} m^{-3}). The high number densities reduce the average distance between mobile point defects and SFTs, thereby enabling SFTs to absorb

mobile SIAs more efficiently. This remains true even though the impact range and sink strength of a single SFT are smaller than those of a loop or a straight dislocation (details in Supplementary Fig. 1). The high density of SFTs can be attributed to high probability for direct formation within energetic displacement cascades. This is generally considered a result of the low stacking fault energy (SFE) in fcc copper[27,35]. With increasing temperatures, SFTs will annihilate due to their interaction with mobile SIAs or thermally evaporations[50]. This leads to the experimentally observed decrease of SFT densities with increasing temperatures[57]. Additionally, the impact of non-perfect SFTs on the predicted swelling rate is also estimated and the bias values are found to be close to those of perfect SFTs, which are substantially higher than those of other types of sinks.

The swelling rates in scenario (ii) exhibit a close agreement with the average values of experimental observations (from around 0.1 to 0.5% dpa^{-1})[12,29,33–44], as demonstrated by the blue curve in Fig. 4. The 1/3 < 111 > {111} interstitial loop is assumed as the governing type of sink in this scenario, the sink strengths of which are normally higher than those of straight dislocations, as demonstrated in Fig. 5b. The presence of loops, compared with scenario (i), reduces the swelling rate under 700 K. For instance, the swelling rates observed by Zinkle et al.[29] and Singh et al.[33–35] under 600 K in Fig. 4 (circled in orange) are lower than the predicted swelling rates that only consider SFTs. Here, the collective effect of the low bias dislocation loops with their number densities (generally higher than 10^{20} m^{-3} under 600 K[29,42,57]) is evident in experimental observations. Notably, the number density of both SFTs and dislocation loops decreases with increasing temperature, leading to a weaker effect of scenarios (i) and (ii) at high temperatures under a void swelling regime.

In scenario (iii), the contribution of straight dislocations on the swelling rates prevails, especially at high temperatures (approximately above 700 K). This dislocation-dominant scenario represents the predicted lower limit of the swelling rates of irradiated copper. The sink strengths of dislocations decrease not as much as those of SFTs or loops with increasing temperatures (as shown in Fig. 4c). These temperature-insensitive sink strengths can be attributed to the stable dislocation densities observed in experiments, mostly ranging between 10^{12} and 10^{13} m^{-2}[12,29,34–36,41,42], with only a few experiments reporting higher dislocation densities (over 10^{13} m^{-2})[43,44,61]. Comparatively, the number densities and sink strengths of SFTs and loops decrease significantly with increasing temperatures based on experimental observations[29,41,57,61]. Thus, the role of dislocations in the swelling phenomena observed in fcc copper is more consistent than that of SFTs and loops. Furthermore, since dislocation bias values alone cannot fully explain the observed differences in swelling rates between bcc and fcc materials, it is possible that SFTs are the primary factor determining these swelling rate differences.

Additionally, at such high temperatures, vacancy evaporations impact swelling phenomena significantly[22,67,68], which takes place from the void surface. When the temperature is lower than 548 K, no more than 10% of the vacancies in voids will evaporate; yet this ratio reaches 60% when the temperature is 771 K. The equations for evaporation rate calculations are provided in Supplementary Note 1 and Supplementary Fig. 4. Additional experimental data is summarized in Supplementary Figs. 2 and 3 as a reference.

Methods

Construction of sinks and strain calculations

The construction of the sinks was performed using the LAMMPS molecular dynamics code[69] with interatomic potential developed by Mishin et al.[70]. Perfect SFTs with 1.5 nm, 2.0 nm, and 3.5 nm in size were formed by relaxing a triangular 1/3<111> vacancy loop containing 21, 36, and 105 vacancies, respectively. A non-perfect SFT with a size of ~2 nm (containing 32 vacancies) was generated from a perfect 2 nm SFT (containing 36 vacancies) by absorbing four mobile SIAs. The 1/3<111> interstitial dislocation loop of 10 nm size was set up with 223 inserted SIAs on the <111> plane. The 10 nm void was built up by removing 44115 atoms in a spherical shape. The coordinates were $[1\bar{1}0]$, $[11\bar{2}]$, and [111] for the simulation boxes

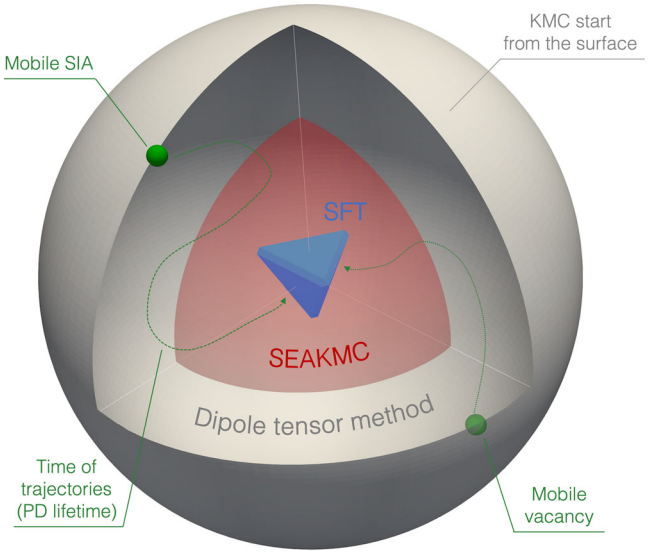

Fig. 6 | Scheme of the simulation system. Point defects (green spheres) start their diffusions from the edge of the system and end up being absorbed by the SFT (the blue tetrahedron). MEBs in the core region are calculated using SEAKMC.

of sinks above, with periodic boundary conditions in all directions. Both the edge and screw dislocations were 1/2<110>{111} type, which dissociated into two 1/6<112> partial dislocations. The strain fields were calculated using OVITO[71] visualization and analysis code.

Atomistic kinetic Monte Carlo (AKMC)

The bias of different types of sinks was calculated using a recently developed AKMC approach[30,31], the scheme of which is shown in Fig. 6. The KMC processes of point defect diffusion starts from the spherical surface of the simulation system, where the distance to the center of the biased sink remains the same. The lifetime of a point defect, which is defined as the time required to diffuse from an initial position to a sink, was then calculated based on the KMC simulation. The time of point defect diffusion to the first nearest neighbor depends on the migration energy barriers (MEBs), which are mostly calculated using SEAKMC[72,73]. Dipole tensor method[65,74] was employed to calculate the MEBs far from the sink[30]. Detailed approaches for the MEB calculation are provided in Supplementary Note 2 and the results are shown from Supplementary Figs. 13–28. The bias based on the lifetime is derived,

$$Bias = \frac{Z_i - Z_v}{Z_v} = \frac{\frac{\tau_i^r}{\tau_i} - \frac{\tau_v^r}{\tau_v}}{\frac{\tau_v^r}{\tau_v}} = \frac{\tau_i^r \tau_v}{\tau_v^r \tau_i} - 1, \quad (1)$$

where τ_i and τ_v represents the lifetime of SIAs and vacancies, and the superscript r means random walk. Z_i and Z_v stand for capture efficiencies of SIAs and vacancies to the sink[22]. Plus, the sink strength in the physical system[75] is calculated using

$$k_\alpha^2 = Z_\alpha k^2, \quad (2)$$

where α is either i or v, representing interstitials and vacancies, respectively. The sink strength without the influence of the interaction between the sink and the point defect, k^2, is obtained during AKMC calculations,

$$k^2 = \frac{2n}{d_j^2 \langle n_j \rangle}, \quad (3)$$

where n is the dimensionality ($n = 3$ in this study), $\langle n_j \rangle$ is the average number of jumps of PDs, and d_j is the jump distance[76,77]. Notably, the sink

strength for voids is obtained based on rate theory[22],

$$k^2 = 4\pi\langle R\rangle\rho, \tag{4}$$

where $\langle R\rangle$ represents the average void radius and ρ is the void density. The reason to employ this equation is the significant impact of both void size and density on the sink strength. However, it is challenging to obtain accurate void sink strength considering a wide range of sizes, especially considering the evidence that small voids are biased sinks for mobile point defects[4,78–82].

Swelling rate calculation

Swelling rate calculation was derived[22,30,83] and calculated based on the sink strength for comparison with experimental results. When considering only one type of sink, taking SFT as an example (scenario (i)),

$$\text{Swelling rate} = \varepsilon * \frac{k^2_{Void,v}(k^2_{Void,i}+k^2_{SFT,i}) - k^2_{Void,i}(k^2_{Void,v}+k^2_{SFT,v})}{\left(k^2_{Void,v}+k^2_{SFT,v}\right)\left(k^2_{Void,i}+k^2_{SFT,i}\right)} * \left(1-\frac{J^{em}_v}{N}\right). \tag{5}$$

The term $k^2_{sink,\alpha}$ represents the sink strength of a specific sink (void or SFT in this equation) in the ideal system. Subscript α can represent either interstitials with i or vacancies with v, respectively. Survival fraction ε is selected to be 0.1 based on recent analyses to correct for correlated defect recombination[84]. For scenarios (ii) and (iii), k^2_{SFT} was replaced with the sink strength of loops and dislocations. J^{em}_v is the vacancy emission rate[22,68], and N is the number of vacancies contained in a void. J^{em}_v/N is the total volume loss rate of a void.

Dual-ion irradiation of polycrystalline copper

High-purity (99.99%) polycrystalline copper disks obtained from Johnson–Mathey were cold rolled to achieve a 50% reduction in thickness. Prior irradiation, the disks were mechanically and electropolished at −40°C using a 33% HNO_3/67% CH_3OH solution with a 5 V applied potential. A thermocouple wire was spot welded to the back of the TEM disks to monitor the irradiation temperature. Oak Ridge dual-beam Van de Graaff irradiation facilities[85] were used for irradiation. Simultaneous dual-ion beam (4 MeV Fe & 0.2–0.4 MeV He ions) irradiation was conducted at 440 °C, reaching a peak damage level of 13 dpa and helium concentration of 48 appm at a depth of approximately 1.2 µm, as calculated with $E_d = 30$ eV for Cu according to SRIM 2013 Q-C vacancy.txt method[86]. The total fluence of the Fe ion beam was 9.5×10^{19}, and the dose rate was 3.3×10^{-3} dpa/s. The helium beam energy was ramped from 0.2 to 0.4 MeV at 0.025 Hz, resulting in uniform helium implantation at depths of 0.5–1.1 µm.

STEM Experiments

The STEM imaging and 4D-STEM exit-wave power-cepstrum (EWPC) measurements were conducted using a JEOL NEOARM aberration-corrected STEM operating at an acceleration voltage of 200 kV. Atomic-resolution STEM imaging was performed with a semi-convergence angle of ~13.6 mrad and 4D-STEM data for EWPC measurements was acquired using a ~3.4 mrad semi-convergence angle, resulting in a probe diameter of <1 nm. CBED patterns were captured with the beam direction aligned along a Cu $\langle 1\bar{1}0\rangle$ zone axis on a pnCCD pixelated detector with a frame size of 264×264 pixels, an acquisition rate of 1000 frames per second, and at 512×512 real space probe positions. The data was binned by four in each real space dimension to increase the signal-to-noise ratio of the CBED patterns and by an additional two in each reciprocal space dimension to enhance the data processing rate. Details of the EWPC method used to make lattice strain measurements are available in a separate report[55] and related codes are available at https://github.com/ElliotPadgett/PC-STEM.

Data availability

The raw data (migration energy barriers) that supports the findings of this study are available in Figshare with the https://doi.org/10.6084/m9.figshare.24480862. All the other data generated during and/or analyzed during the current study are available from the corresponding author upon reasonable request.

Received: 28 December 2023; Accepted: 3 April 2024;
Published online: 16 April 2024

References

1. Bhattacharya, A. & Zinkle, S. J. in *Comprehensive Nuclear Materials* Vol. 1 (eds Konings, R. J. M. & Stoller, R. E.) 406–455 (Elsevier, 2020).
2. Cawthorne, C. & Fulton, E. J. Voids in irradiated stainless steel. *Nature* **216**, 576–577 (1967).
3. Pugh, S. F. Voids formed by irradiation of reactor materials - report of conference. *J. Br. Nucl. Energy Soc.* **10**, 159 (1971).
4. Mansur, L. K. Void swelling in metals and alloys under irradiation - assessment of theory. *Nucl. Technol.* **40**, 5–34 (1978).
5. Zinkle, S. J. & Was, G. S. Materials challenges in nuclear energy. *Acta Mater.* **61**, 735–758 (2013).
6. Garner, F. A., Toloczko, M. B. & Sencer, B. H. Comparison of swelling and irradiation creep behavior of fcc-austenitic and bcc-ferritic/martensitic alloys at high neutron exposure. *J. Nucl. Mater.* **276**, 123–142 (2000).
7. Du, C. et al. Ultrastrong nanocrystalline steel with exceptional thermal stability and radiation tolerance. *Nat. Commun.* **9**, 5389 (2018).
8. Eswarappa Prameela, S. et al. Materials for extreme environments. *Nat. Rev. Mater.* **8**, 81–88 (2023).
9. Zhang, Z. et al. Nanoscale origins of the damage tolerance of the high-entropy alloy CrMnFeCoNi. *Nat. Commun.* **6**, 10143 (2015).
10. Gao, P. et al. The critical role of point defects in improving the specific capacitance of delta-MnO_2 nanosheets. *Nat. Commun.* **8**, 14559 (2017).
11. Lee, W. et al. Perovskite microcells fabricated using swelling-induced crack propagation for colored solar windows. *Nat. Commun.* **13**, 1946 (2022).
12. Zinkle, S. J. & Farrell, K. Void swelling and defect cluster formation in reactor-irradiated copper. *J. Nucl. Mater.* **168**, 262–267 (1989).
13. Golubov, S. I., Singh, B. N. & Trinkaus, H. Defect accumulation in fee and bcc metals and alloys under cascade damage conditions - towards a generalisation of the production bias model. *J. Nucl. Mater.* **276**, 78–89 (2000).
14. Matsui, H., Gelles, D. S. & Kohno, Y. Large swelling observed in a V-5atmospheric-percent Fe alloy after irradiation in Fftf. *Eff. Radiat. Mater. 15th Int. Symp.* **1125**, 928–941 (1992).
15. Zinkle, S. J. & Snead, L. L. Designing radiation resistance in materials for fusion energy. *Annu. Rev. Mater. Res.* **44**, 241–267 (2014).
16. English, C. A. Low-dose neutron-irradiation damage in Fcc and Bcc metals. *J. Nucl. Mater.* **108**, 104–123 (1982).
17. Victoria, M. et al. The microstructure and associated tensile properties of irradiated fcc and bcc metals. *J. Nucl. Mater.* **276**, 114–122 (2000).
18. Baluc, N. et al. A comparison of the microstructure and tensile behaviour of irradiated fcc and bcc metals. *Microstruct. Process. Irradiat. Mater.* **540**, 539–548 (1999).
19. Brailsford, A. D. & Bullough, R. Rate theory of swelling due to void growth in irradiated metals. *J. Nucl. Mater.* **44**, 121–135 (1972).
20. Wolfer, W. G. The dislocation bias. *J. Comput. Aided Mater. Des.* **14**, 403–417 (2007).
21. Bullough, R., Eyre, B. L. & Krishan, K. Cascade damage effects on swelling of irradiated materials. *Proc. R. Soc. Lond. Ser. A Math. Phys. Eng. Sci.* **346**, 81–102 (1975).
22. Golubov, S. I., Barashev, A. V. & Stoller, R. E. Radiation damage theory. In *Comprehensive Nuclear Materials, Vol 1: Basic Aspects of*

Radiation Effects in Solids/Basic Aspects of Multi-Scale Modeling 357–391 (Elsevier, 2012).
23. Singh, B. N. & Evans, J. H. Significant differences in defect accumulation behavior between Fcc and Bcc crystals under cascade damage conditions. *J. Nucl. Mater.* **226**, 277–285 (1995).
24. Trinkaus, H., Singh, B. N. & Foreman, A. J. E. Impact of glissile interstitial loop production in cascades on defect accumulation in the transient. *J. Nucl. Mater.* **206**, 200–211 (1993).
25. Osetsky, Y. N., Bacon, D. J., Gao, F., Serra, A. & Singh, B. N. Study of loop-loop and loop-edge dislocation interactions in bcc iron. *J. Nucl. Mater.* **283**, 784–788 (2000).
26. Xu, H. X., Osetsky, Y. N. & Stoller, R. E. Cascade annealing simulations of bcc iron using object kinetic Monte Carlo. *J. Nucl. Mater.* **423**, 102–109 (2012).
27. Schaublin, R., Yao, Z., Baluc, N. & Victoria, M. Irradiation-induced stacking fault tetrahedra in fcc metals. *Philos. Mag.* **85**, 769–777 (2005).
28. Yoshida, N., Akashi, Y., Kitajima, K. & Kiritani, M. Formation of secondary defects in copper by 14 Mev neutron-irradiation and their effects on microstructure evolution. *J. Nucl. Mater.* **133**, 405–409 (1985).
29. Zinkle, S. J. & Snead, L. L. Microstructure of copper and nickel irradiated with fission neutrons near 230-degrees-C. *J. Nucl. Mater.* **225**, 123–131 (1995).
30. Yu, Z. & Xu, H. Dislocation loop bias and void swelling in irradiated α-iron from mesoscale and atomistic simulations. *Commun. Mater.* **4**, 29 (2023).
31. Hao, J. N., Casillas-Trujillo, L. & Xu, H. X. Using lifetime of point defects for dislocation bias in bcc Fe. *Curr. Opin. Solid State Mater. Sci.* **26** 101021 (2022).
32. Silcox, J. & Hirsch, P. B. Direct observations of defects in quenched gold. *Philos. Mag.* **4**, 72–89 (1959).
33. Singh, B. N., Leffers, T. & Horsewell, A. Dislocation and void segregation in copper during neutron-irradiation. *Philos. Mag. A Phys. Condens. Matter Struct. Defects Mech. Prop.* **53**, 233–242 (1986).
34. Singh, B. N., Horsewell, A., Toft, P. & Edwards, D. J. Temperature and dose dependencies of microstructure and hardness of neutron-irradiated Ofhc copper. *J. Nucl. Mater.* **224**, 131–140 (1995).
35. Singh, B. N., Eldrup, M., Horsewell, K., Ehrhart, P. & Dworschak, F. On recoil energy dependent void swelling in pure copper - part I. Experimental results. *Philos. Mag. A Phys. Condens. Matter Struct. Defects Mech. Prop.* **80**, 2629–2650 (2000).
36. Mukouda, I. & Shimomura, Y. Damage evolution in neutron-irradiated Cu during neutron irradiation. *J. Nucl. Mater.* **271**, 230–235 (1999).
37. Brager, H. R. Effects of neutron-irradiation to 63 Dpa on the properties of various commercial copper-alloys. *J. Nucl. Mater.* **141**, 79–86 (1986).
38. Lee, T. S. et al. Microstructural evolution and swelling of high-strength, high conductivity Rs-Pm copper-alloys irradiated to 13.5 Dpa with neutrons. *J. Nucl. Mater.* **141-143**, 179–183 (1986).
39. Livak, R. J., Zocco, T. G. & Hobbs, L. W. Neutron damage microstructures of high-conductivity copper-alloys. *J. Nucl. Mater.* **144**, 121–127 (1987).
40. Garner, F. A., Brager, H. R. & Anderson, K. R. Neutron-induced changes in density and electrical-conductivity of copper-alloys at 16 to 98 Dpa and 430-degrees-C. *J. Nucl. Mater.* **179**, 250–253 (1991).
41. Singh, B. N., Horsewell, A., Gelles, D. S. & Garner, F. A. Void swelling in copper and copper-alloys irradiated with fission neutrons. *J. Nucl. Mater.* **191**, 1172–1176 (1992).
42. Singh, B. N., Eldrup, M., Zinkle, S. J. & Golubov, S. I. On grain-size-dependent void swelling in pure copper irradiated with fission neutrons. *Philos. Mag. A Phys. Condens. Matter Struct. Defects Mech. Prop.* **82**, 1137–1158 (2002).
43. Muroga, T. & Yoshida, N. Microstructure of neutron-irradiated copper alloyed with nickel and zinc. *J. Nucl. Mater.* **212**, 266–269 (1994).
44. Watanabe, H. & Garner, F. A. Void swelling of pure copper, Cu-5ni and Cu-5mn alloys irradiated with fast-neutrons. *J. Nucl. Mater.* **212**, 370–374 (1994).
45. Brimhall, J. L. & Kissinger, H. E. Void formation in irradiated copper, nickel, and copper-nickel alloys. *Radiat. Effects: Inc. Plasma Sci. Plasma Technol.* **15**, 259–272 (1972).
46. Garner, F. A., Hamilton, M. L., Shikama, T., Edwards, D. J. & Newkirk, J. W. Response of solute and precipitation strengthened copper-alloys at high neutron exposure. *J. Nucl. Mater.* **191**, 386–390 (1992).
47. Muroga, T., Matue, T., Watanabe, H. & Yoshida, N. Void swelling of copper and copper alloys induced by heavy ion irradiation. *Eff. Radiat. Mater. 18th Int. Symp.* **1325**, 991–998 (1999).
48. Yamakawa, K., Mukouda, I. & Shimomura, Y. Void formation in neutron-irradiated Cu and Cu alloys. *J. Nucl. Mater.* **191**, 396–400 (1992).
49. Zinkle, S. J. & Singh, B. N. Microstructure of Cu-Ni alloys neutron irradiated at 210 degrees C and 420 degrees C to 14 dpa. *J. Nucl. Mater.* **283**, 306–312 (2000).
50. Singh, B. N., Golubov, S. I., Trinkaus, H., Edwards, D. J. & Eldrup, M. Review: evolution of stacking fault tetrahedra and its role in defect accumulation under cascade damage conditions. *J. Nucl. Mater.* **328**, 77–87 (2004).
51. Ishino, S., Sekimura, N., Hirooka, K. & Muroga, T. Insitu observation of cascade damage in gold under heavy-ion irradiation at high-temperature. *J. Nucl. Mater.* **141**, 776–780 (1986).
52. Kiritani, M. et al. Formation of vacancy clustered defects from cascade collisions during heavy-ion irradiation and their annihilation by freely-migrating interstitial atoms. *J. Nucl. Mater.* **212-215**, 192–197 (1994).
53. Martínez, E. & Uberuaga, B. P. Mobility and coalescence of stacking fault tetrahedra in Cu. *Sci. Rep.* **5**, 9084 (2015).
54. Yu, Z. H., Muller, D. A. & Silcox, J. Study of strain fields at a-Si/c-Si interface. *J. Appl. Phys.* **95**, 3362–3371 (2004).
55. Padgett, E. et al. The exit -wave power-cepstrum transform for scanning nanobeam electron diffraction: robust strain mapping at subnanometer resolution and subpicometer precision. *Ultramicroscopy* **214**, 112994 (2020).
56. Zinkle, S. J., Farrell, K. & Kanazawa, H. Microstructure and cavity swelling in reactor-irradiated dilute copper-boron alloy. *J. Nucl. Mater.* **179**, 994–997 (1991).
57. Singh, B. N. & Zinkle, S. J. Defect accumulation in pure fcc metals in the transient regime - a review. *J. Nucl. Mater.* **206**, 212–229 (1993).
58. Osetsky, Y. N., Serra, A., Victoria, M., Golubov, S. I. & Priego, V. Vacancy loops and stacking-fault tetrahedra in copper - I. Structure and properties studied by pair and many-body potentials. *Philos. Mag. A Phys. Condens. Matter Struct. Defects Mech. Prop.* **79**, 2259–2283 (1999).
59. Golubov, S. I., Singh, B. N. & Trinkaus, H. On recoil-energy-dependent defect accumulation in pure copper - part II. Theoretical treatment. *Philos. Mag. A Phys. Condens. Matter Struct. Defects Mech. Prop.* **81**, 2533–2552 (2001).
60. Hirsch, P. B., Cotterill, R. M. J. & Jones, M. W. in *Proc. 5th International Congress on Electron Microscopy* (Academic Press, 1962).
61. Leffers, T., Singh, B. N., Buckley, S. N. & Manthorpe, S. A. Void-swelling in cold-worked copper during Hvem irradiation. *J. Nucl. Mater.* **118**, 60–67 (1983).
62. Chang, Z. W., Olsson, P., Terentyev, D. & Sandberg, N. Dislocation bias factors in fcc copper derived from atomistic calculations. *J. Nucl. Mater.* **441**, 357–363 (2013).
63. Skinner, B. C. & Woo, C. H. Shape effect in the drift diffusion of point-defects into straight dislocations. *Phys. Rev. B* **30**, 3084–3097 (1984).
64. Fisher, S. B., White, R. J. & Miller, K. M. Quantitative-analysis of void swelling in pure copper. *Philos. Mag. A Phys. Condens. Matter Struct. Defects Mech. Prop.* **40**, 239–255 (1979).

65. Seif, D. & Ghoniem, N. M. Effect of anisotropy, SIA orientation, and one-dimensional migration mechanisms on dislocation bias calculations in metals. *J. Nucl. Mater.* **442**, S633–S638 (2013).
66. Sivak, A. B. & Sivak, P. A. Efficiency of dislocations as sinks of radiation defects in fcc copper crystal. *Crystallogr. Rep.* **59**, 407–414 (2014).
67. Was, G. S. *Fundamentals of Radiation Materials Science: Metals and Alloys* (Springer, 2007).
68. Barashev, A. V., Golubov, S. I., Osetsky, Y. N. & Stoller, R. E. Dissociation of migrating particle from trap with long-range interaction field. *Philos. Mag.* **90**, 907–921 (2010).
69. Plimpton, S. Fast parallel algorithms for short-range molecular-dynamics. *J. Comput. Phys.* **117**, 1–19 (1995).
70. Mishin, Y., Mehl, M. J., Papaconstantopoulos, D. A., Voter, A. F. & Kress, J. D. Structural stability and lattice defects in copper: Ab initio, tight-binding, and embedded-atom calculations. *Phys. Rev. B* **63**, 224106 (2001).
71. Stukowski, A. Visualization and analysis of atomistic simulation data with OVITO-the Open Visualization Tool. *Model. Simul. Mater. Sci. Eng.* https://doi.org/10.1088/0965-0393/18/1/015012 (2010).
72. Xu, H. X., Osetsky, Y. N. & Stoller, R. E. Self-evolving atomistic kinetic Monte Carlo: fundamentals and applications. *J. Phys. Condens. Mater.* https://doi.org/10.1088/0953-8984/24/37/375402 (2012).
73. Xu, H. X., Stoller, R. E., Beland, L. K. & Osetsky, Y. N. Self-evolving atomistic kinetic Monte Carlo simulations of defects in materials. *Comp. Mater. Sci.* **100**, 135–143 (2015).
74. Carpentier, D., Jourdan, T., Le Bouar, Y. & Marinica, M. C. Effect of saddle point anisotropy of point defects on their absorption by dislocations and cavities. *Acta Mater.* **136**, 323–334 (2017).
75. Mansur, L. K., Brailsford, A. D. & Wolfer, W. G. On the meaning of sink capture efficiency and sink strength for point-defects. *J. Nucl. Mater.* **105**, 36–38 (1982).
76. Heinisch, H. L., Singh, B. N. & Golubov, S. I. The effects of one-dimensional glide on the reaction kinetics of interstitial clusters. *J. Nucl. Mater.* **283**, 737–740 (2000).
77. Malerba, L., Becquart, C. S. & Domain, C. Object kinetic Monte Carlo study of sink strengths. *J. Nucl. Mater.* **360**, 159–169 (2007).
78. Dubinko, V. I., Ostapchuk, P. N. & Slezov, V. V. Theory of radiation-induced and thermal coarsening of the void ensemble in metals under irradiation. *J. Nucl. Mater.* **161**, 239–260 (1989).
79. Dubinko, V. I., Guglya, A. G. & Donnelly, S. E. Radiation-induced formation, annealing and ordering of voids in crystals: theory and experiment. *Nucl. Instrum. Methods Phys. Res. Sec. B Beam Interact. Mater. At.* **269**, 1634–1639 (2011).
80. Ayanoglu, M. & Motta, A. T. Void shrinkage in 21Cr32Ni austenitic model alloy during in-situ ion irradiation. *J. Nucl. Mater.* **543**, 152636 (2021).
81. Chen, Y. et al. Damage-tolerant nanotwinned metals with nanovoids under radiation environments. *Nat. Commun.* **6**, 7036 (2015).
82. Niu, T. et al. Recent studies on void shrinkage in metallic materials subjected to in situ heavy ion irradiations. *Jom* **72**, 4008–4016 (2020).
83. Mansur, L. K. Theory and experimental background on dimensional changes in irradiated alloys. *J. Nucl. Mater.* **216**, 97–123 (1994).
84. Zinkle, S. J. & Stoller, R. E. Quantifying defect production in solids at finite temperatures: thermally-activated correlated defect recombination corrections to DPA (CRC-DPA). *J. Nuclear Mater.* https://doi.org/10.1016/j.jnucmat.2023.154292 (2023).
85. Zinkle, S. J. Dual-ion irradiation of copper. 86–89 (ORNL report, 1987).
86. Lin, Y.-R., Zinkle, S. J., Ortiz, C. J., Webb, R. & Stoller, R. E. Predicting displacement damage for ion irradiation: origin of the overestimation of vacancy production in SRIM full-cascade calculations. *Curr. Opin. Solid State Mater. Sci*. **27**, 101120 (2023).

Acknowledgements

This work is supported by the US Department of Energy, Office of Science, Basic Energy Sciences, under Award No. DE-SC0019151. This research used resources of the National Energy Research Scientific Computing Center, a DOE Office of Science User Facility supported by the Office of Science of the US Department of Energy under Contract No. DE-AC02-05CH11231. The scanning transmission electron microscopy portion of this research was supported by the Center for Nanophase Materials Sciences (CNMS), which is a U.S. Department of Energy, Office of Science User Facility at Oak Ridge National Laboratory (ORNL). This research was also funded by the US Department of Energy's Fusion Materials Program at Oak Ridge National Laboratory, under the contract DE-AC05-00OR22725 with UT-Battelle, LLC.

Author contributions

Ziang Yu: Investigation, Methodology, Validation, Formal analysis, Writing – original draft, Visualization. Yan-Ru Lin: Experimental observation, Formal analysis, Writing – review & editing. Michael J. Zachman: Experimental observation, Formal analysis, Writing – review & editing. Steven J. Zinkle: Methodology, Formal analysis, Writing – review & editing, Supervision. Haixuan Xu: Conceptualization, Methodology, Formal analysis, Writing – review & editing, Supervision, Project administration, Funding acquisition.

Competing interests

The authors declare no competing interests.

Additional information

Supplementary information The online version contains supplementary material available at https://doi.org/10.1038/s43246-024-00491-7.

Correspondence and requests for materials should be addressed to Haixuan Xu.

Peer review information *Communications Materials* thanks Weizhong Han and the other, anonymous, reviewer(s) for their contribution to the peer review of this work. Primary Handling Editors: Xiaoyan Li and John Plummer.